A 10.8 mW Body Channel Communication/MICS Dual-Band Transceiver for a Unified Body Sensor Network Controller

Namjun Cho, *Student Member, IEEE*, Joonsung Bae, *Student Member, IEEE*, and Hoi-Jun Yoo, *Fellow, IEEE*

***Abstract*—An energy-efficient dual-band transceiver for unified body sensor network is presented. The transceiver provides 30–70 MHz body channel communication (BCC) and 402–405 MHz medical implant communication service (MICS). For low energy consumption, the BCC and MICS band circuits in the receiver operate concurrently with their front-ends shared. As a result, up to 30% energy saving is achieved. The dual-band front-end circuits consist of a cascaded *LC* tank LNA and a current-recycling concurrent-down conversion mixer. The proposed LNA provides $>$ 16 dB gains both in the BCC and MICS bands and suppresses interferences coupled through the human body by more than 10 dB. For BCC robustness, a variable adaptive frequency hopping is applied. The transceiver fabricated with 0.18 μm CMOS is fully compatible with the FCC regulations for MICS and consumes 10.8 mW and 4.9 mW in its RX and TX modes, respectively. The adjacent channel rejections are measured at $>$ 30 dB in the dual-bands.**

***Index Terms*—Body channel communication, concurrent operation, dual-band transceiver, medical implant communication service (MICS), unified body sensor network.**

I. Introduction

BODY sensor network (BSN) provides wireless connectivity among various physiological sensors and medical devices carried by a patient for the continuous and ambulatory health care. Basically, the BSN is categorized into wearable and implantable sensor networks. The wearable BSN is only for communication among the on-body health monitoring devices such as electrocardiogram (ECG), body temperature, and saturation of peripheral oxygen (SpO2) sensors. The implantable BSN connects the implanted electronics such as pacemaker and neuro-stimulator with an external controller. These two types of BSN have been studied and developed separately. However, the recent interest is combining the wearable and implantable BSNs together to provide more convenient and inexpensive health care service. The IEEE 802.15 task group for the BSN standardization is also discussing the unified BSN concept actively [1].

Fig. 1 presents the overall structure of the unified BSN which consists of a network controller attached to human skin and multiple sensors deployed on and inside the human body [2]. The on-body network controller plays significant roles in terms of the patient mobility and the energy consumption. As the network master of the star BSN, it collects vital data sensed by each node and processes them. After the sufficient amount of data is gathered, the controller wirelessly transmits them to a remote access point which is 10–100 m away from the patient. As a result, the coverage of the health care service can be extended without increasing sensitivity of the power-hungry sensor radios. For in-body communication inside the BSN, the controller operates as a wireless repeater. Because internal organs of the human body have the conductivity (σ) larger than 0.5 S/m, the strength (E) of the electromagnetic field traveling through the body attenuates exponentially with distance (z) as shown in (1) [3]:

$$E = E_0 \exp\left(-\sqrt{\frac{\omega\mu\sigma}{2}}z\right) \begin{cases} E_0 : \text{Field strength at } z = 0 \\ \omega : \text{Field frequency} \\ \mu = 4\pi \times 10^{-7}. \end{cases} \tag{1}$$

For 2 m communication between the implanted devices, their wireless transceivers using the medical implant communication service (MICS) band around 400 MHz should have at least -90 dBm sensitivity as shown in Fig. 2. According to the previous study, this sensitivity can be hardly obtained with less than 5 mW power consumption [4]. On the other hand, the on-body controller receives data from the source implant in the middle of the signal path and retransmits them to the destination node with the regenerated power. Hence, the maximum distance of the communication through the human body is less than 1 m, and the minimum detectable power of the MICS radio is enough with -70 dBm which can be achieved with sub-mW power consumption [5]. In summary, the unified BSN of Fig. 1 minimizes the energy consumption of the implantable and wearable sensor

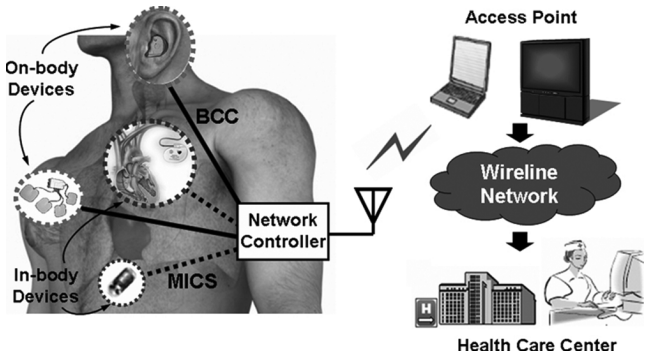

Fig. 1. Unified body sensor network.

Manuscript received April 15, 2009; revised August 13, 2009. Current version published December 11, 2009. This paper was approved by Guest Editor Vadim Gutnik.

The authors are with the Department of Electrical Engineering and Computer Science, Korea Advanced Institute of Science and Technology (KAIST), Daejeon 305-701, Korea (e-mail: buzm@eeinfo.kaist.ac.kr; joonsung@eeinfo.kaist.ac.kr; hjyoo@ee.kaist.ac.kr)

Digital Object Identifier 10.1109/JSSC.2009.2032592

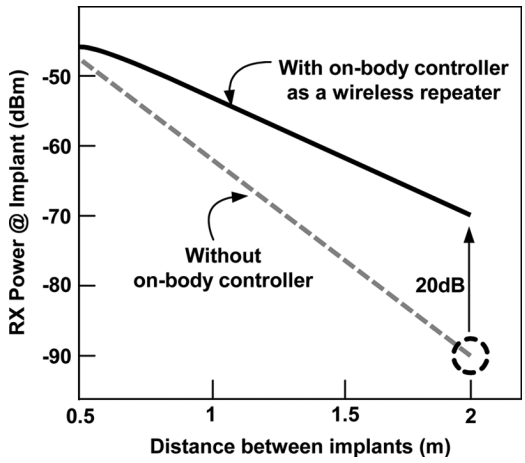

Fig. 2. Sensitivity requirement of implanted MICS radios.

nodes by concentrating the communication power to the network controller. Due to the limited energy capacity of small batteries used for the sensor nodes, the star topology makes more sense in the BSN.

This work focuses on the implementation of an energy-efficient transceiver integrated in the versatile network controller. The transceiver should operate in dual-modes. First, it follows the MICS regulations claimed by FCC to communicate with the implanted devices [6]. The transceiver also needs to have the function of wireless communication with the wearable sensor nodes. Since there is no standard defining frequency and protocols for the wearable BSN, many wireless transceivers integrated in the on-body sensors used the unlicensed ISM band of 1 or 2.4 GHz [7], [8]. However, it is found that the wireless channel using over 1 GHz frequency shows significant path loss due to the body shadowing effect [9]. Recently, the body channel communication (BCC) which uses the human body as a communication channel has been introduced and optimized for BSN applications [10], [11]. Since the data transfer between the on-body transceivers is done by modulating electrical fields formed around the human body, the signal is not blocked by the conductive human tissue. In addition, BCC can utilize low frequency band under 150 MHz without using a large antenna. This reduces power consumption and size of the transceiver substantially. Therefore, BCC is adopted in this work as the on-body communication method.

The key feature of the proposed dual-band transceiver is that its front end circuits including LNA and mixer can amplify and down-convert the BCC and MICS band signals concurrently without consuming additional current. The sharing of the operating power and time between BCC and MICS saves up to 30% of the total energy. To support the concurrent operation, the LNA employs the cascaded *LC* tanks which resonate in the BCC and MICS bands as its loads. The dual-band mixer recycles half of the current biasing its MICS part to activate its BCC part.

Sections II and III give the system overview and the architecture of the dual-band transceiver, respectively. After discussing

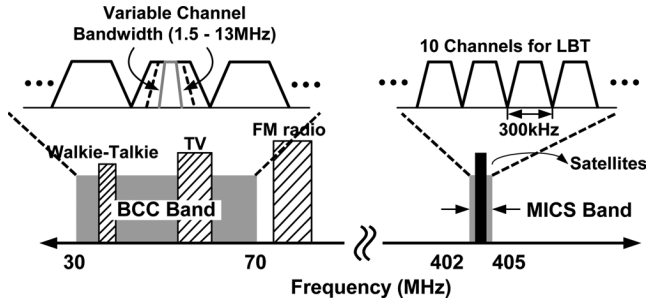

Fig. 3. Frequency bands for BCC/MICS and their channel division.

the detailed design of the building blocks in Section IV, its measurement results will be shown in Section V. Finally, Section VI concludes the paper.

II. System Overview

Fig. 3 shows the frequency bands for MICS and BCC and the channel allocation within each band. The MICS regulation partitions the spectrum from 402 to 405 MHz into 300 kHz channels [6]. Any modulation scheme can be employed in each channel as long as the MICS regulation mask is not violated. The 10 channels are used for the listen-before-talk (LBT) protocol to avoid possible interferences with the primary users such as meteorological and earth exploring satellites. Due to the same reason, the EIRP of a MICS transmitter must not exceed 25 μW or -16 dBm. The 30–70 MHz band selected for BCC can guarantee 10^{-6} BER according to the body channel analysis considering path loss and the FCC emission limit [12]. The interference issue also exists in BCC due to the human body antenna effect [11]. To solve the problem, the adaptive frequency hopping (AFH) technique using fixed 4 channels has been used [11]. AFH continuously monitors status of the channel which is currently used, and selects only clean channels for communication. However, many health care applications require the robust on-body communication even when a number of interferences congest the BCC band. The variable AFH in this work changes the data rate and the channel bandwidth according to interference condition, thereby keeping the number of surviving channels larger than a threshold. The number of hopping channels can be varied from 3 for 5 Mb/s to 20 for 500 kb/s. The FSK modulation is employed in both of the BCC and MICS channels because it shows better spectral efficiency than ASK and requires less complex modem circuits than PSK.

The MICS regulation instructs that the LBT protocol is performed by the procedure presented in Fig. 4. As the first step, the 10 channels in the MICS band are scanned, and the most clean 2 channels among them are selected for communication. Before every starting of the data transaction, the MICS transceiver scans one of the pre-selected channels (CH1) again to check if it is still clean. If the channel proves to be corrupted, the other one (CH2) is scanned as the alternative channel. Only when the channel condition is satisfactory, the data communication can start. After all data transactions, the MICS transceiver enters the ready state. To initiate another MICS communication, 10 channels should be scanned again. Because at least 10 ms for

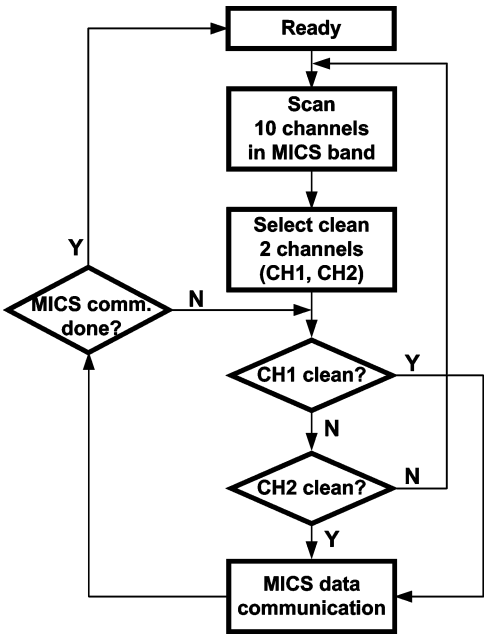

Fig. 4. Listen-before-talk (LBT) procedure.

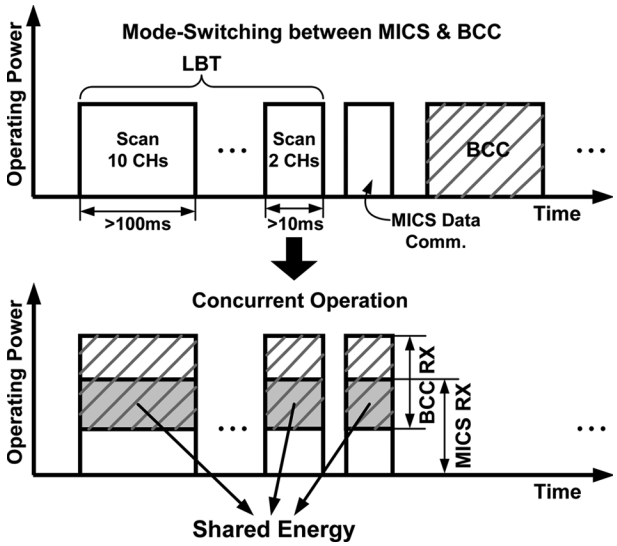

Fig. 5. Concurrent operation of BCC and MICS for energy saving.

each channel scan is mandatory [13], the large amount of energy is wasted for the interference avoidance. The energy for BCC increases the total energy consumption of the transceiver further with the conventional mode-switching between MICS and BCC (Fig. 5). In this work, the energy consumed for the LBT and the MICS data reception is recycled by sharing the front end circuits of the MICS receiver with BCC and receiving the dual-band signals concurrently. The shaded area in Fig. 5 is the product of the time and operating power shared between MICS and BCC, that is, the amount of energy saved in the dual-band transceiver. If the data reception periods for BCC and MICS are matched, the 30% energy reduction can be achieved by the concurrent operation.

III. Transceiver Architecture

Fig. 6 shows the transceiver architecture which consists of the distinct two chains for dual-band operation. The LNA and mixer circuits which consume the largest power are shared between BCC and MICS. The MICS band antenna attached to skin also functions as an electrode that couples BCC signal to the human body. Following the dual-band front ends, the BCC and MICS signals are down-converted to zero and low intermediate frequencies (IF) concurrently. The MICS baseband signal with 300 kHz bandwidth is easily corrupted by 1/f noise generated in the base band circuits. Therefore, The 450 kHz IF for MICS RX is selected to position the desired signal band beyond the 1/f corner frequency. The channel bandwidth of the BCC signal changes for the variable AFH scheme. However, the minimum bandwidth is 1.5 MHz which is far higher than the 1/f corner frequency. The direct-conversion receiver is suitable for BCC because 1/f noise and dc offset can be rejected by a first-order high-pass filter with 700 kHz cutoff frequency without sacrificing the sensitivity. The baseband filter for MICS should be a complex band-pass filter to remove the image signal. The fifth-order complex Butterworth filter is employed to give 38 dB and 48 dB image and adjacent channel rejections. The cutoff frequency of the fourth-order low-pass filter in the BCC baseband chain is programmable for the variable AFH.

The LO signals applied to the dual-band mixer are generated by integer and fractional PLLs. In BCC TX, the BFSK signal is obtained by changing the control current of the CCO according to binary data from the digital circuit. The TX data is DC-free coded not to disturb the channel frequency fixed by negative feedback of the integer PLL. The transconductance of the V/I converter is programmable to make the amplitude of the control current proportional to TX data rate, and thus the modulation index (MI) of the BFSK signal is maintained at 1. In MICS TX, the 16 bit input code to the $\Sigma\Delta$ modulator controls the division ratio of the fractional-N PLL. By changing the code value, the MICS BFSK signal can be generated. The RC/CR network following the *LC* VCO makes the I/Q LO signals applied to the mixer. As the accurate quadratic relation between the I/Q baseband signals is significant for the image rejection, careful considerations in the layout of the passive elements are necessary to enhance the matching property.

IV. Building Blocks

A. Body Interfacing Circuits

The antenna used in the transceiver needs special consideration in its design to support dual-band operation. As an electrode for BCC, the antenna should be attached to skin securely to minimize the contact impedance at the signal interface. Therefore, the small and planar geometry of the antenna is desirable. However, the low-profile designs such as loop and planar inverted F [14] are prohibited because the radiating body of those antennas is shorted to ground at low frequency bands for BCC. Fig. 7 shows the antenna structure that satisfies the requirements mentioned above. The radiating body has spiral shape with the area of 25×18 mm^2. The 30×40 mm^2 ground plane is placed 1.5 mm below the radiating body, and the transceiver chip on the ground area applies FSK signal through the feed. From the top

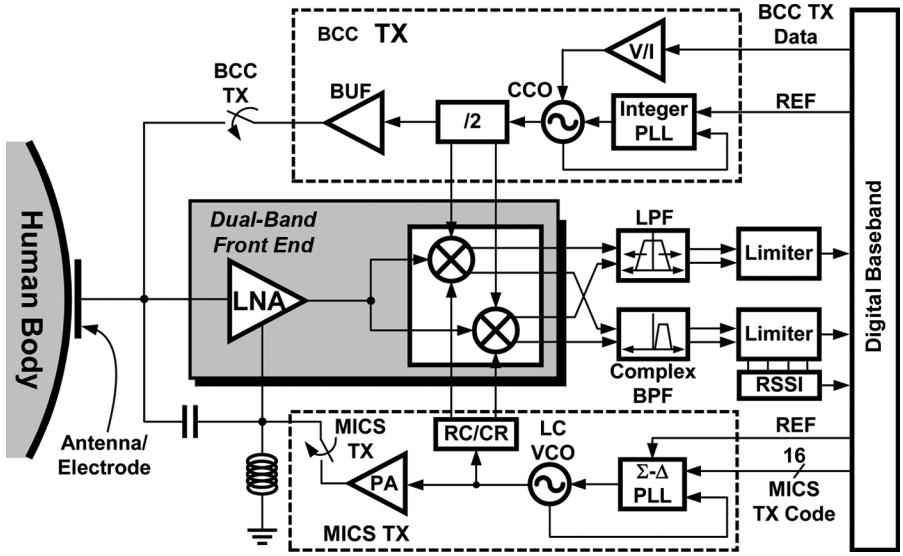

Fig. 6. Transceiver architecture.

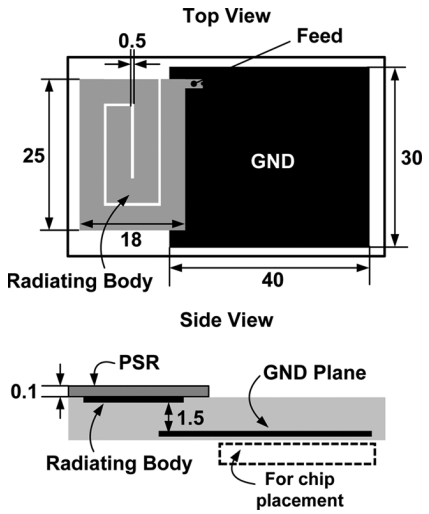

Fig. 7. MICS antenna combined with BCC electrode (all dimensions are in millimeters).

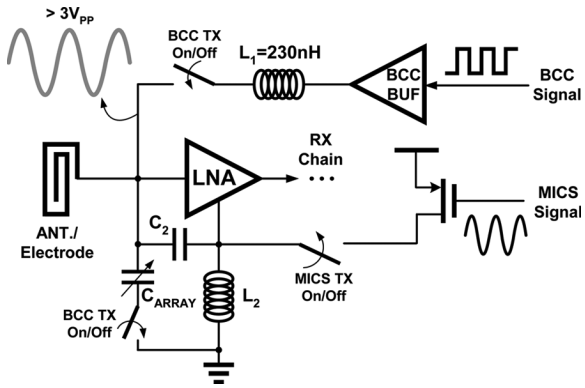

Fig. 8. TX buffers using *LC* resonance.

view, the body and ground planes are placed side-by-side. The fringing effect dominant in this structure increases the effective antenna size and thus the resonant frequency is lowered. The radiating body as the electrode also generates a number of fringing electric fields around it in the BCC band, and thus the strong electric coupling between TX and RX can be formed. Finally, the antenna body which makes direct contact with skin is protected by a 100 μm photo-solder-resist (PSR) layer showing the relative permittivity of 3.2.

Due to the high conductivity and electrical permittivity of the human body, the capacitance of the on-body antenna becomes higher than 10 pF from measurements using a network analyzer. To drive this large capacitor with low power, a 230 nH inductor (L_1) is inserted between the BCC TX buffer and the antenna as shown in Fig. 8. The series resonance by the L_1 and the antenna capacitance boosts swing level of the signal applied to skin to >3 V without using a high supply voltage. Moreover, the BCC buffer only needs to compensate the resistive loss of the resonator to drive the antenna. As a result, 1.2 mW is consumed by the BCC buffer at each frequency from 30 to 70 MHz. This is 60% power reduction compared with the case using no inductor. The capacitor array connected in series with L_1 adjusts the resonant frequency to the center of the BCC channel. The MICS buffer exploits the L_2C_2 tank resonance to boost its load impedance to 250 Ω. The power efficiency of the buffer is improved to 30% from 10% without the resonance network. The L_2 and C_2 are reused in LNA for 50 Ω impedance matching.

B. Cascaded LC Tank LNA

Fig. 9 shows the schematic of the dual-band LNA. The M_1 transistor is inductively degenerated to provide 50 Ω input resistance at 400 MHz. At the BCC frequency band less than 70 MHz, the LNA operates as a simple common-source amplifier because the reactance of L_S becomes negligible. The cascaded *LC* tanks as the load enable dual-band amplification of the LNA. The load impedance $Z(s)$ is calculated as

$$Z(s) = \frac{(L_M + L_B)s + L_M L_B (C_M + C_B)s^3}{(L_M C_M s^2 + 1)(L_B C_B s^2 + 1)} \qquad (2)$$

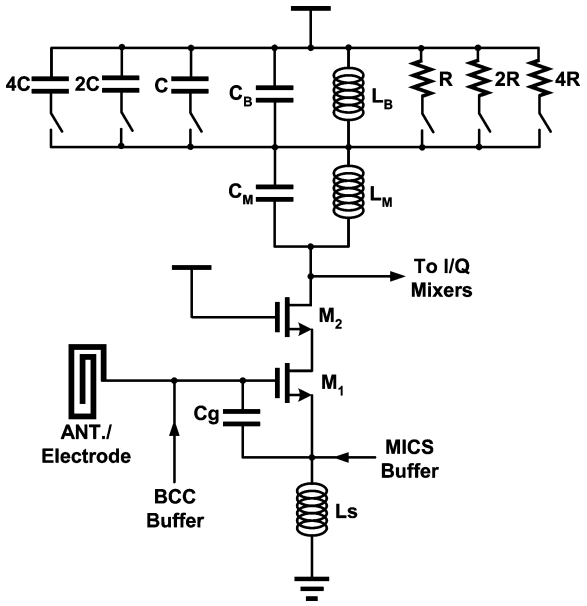

Fig. 9. Cascaded *LC* tank LNA.

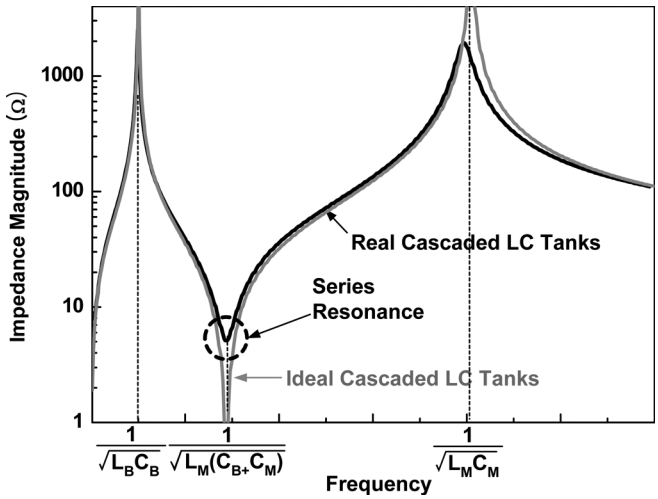

Fig. 10. Impedance curve of the cascaded *LC* tanks.

when parasitic resistances in the inductors and capacitors are ignored. The two tank resonances at $1/\sqrt{L_M C_M}$ and $1/\sqrt{L_B C_B}$ are used to give voltage gains both in the BCC and MICS bands. The cascaded *LC* tanks also generate a series resonance at $1/\sqrt{L_M || L_B(C_M + C_B)}$. With $L_B \gg L_M$, the resonant frequency can be approximated as $1/\sqrt{L_M(C_M + C_B)}$, which appears between the BCC and MICS bands as shown in Fig. 10. This series resonance is quite beneficial to suppress possible interferences at RX and relax linearity requirements of the following circuits. Even though the measured impedance of the cascaded networks is not zero at the series resonance due to finite Q factor of the real inductors, the FM radio signals which are major aggressors to BCC can be attenuated by more than 10 dB. The programmable resistor and capacitor arrays in Fig. 9 control the tank resonant frequency and the Q factor of the $L_B C_B$ tank with eight steps. As a result, the voltage gain of the LNA is maintained as $>$ 16 dB at each channel of the BCC band. Simulations indicate that the LNA shows an NF of 3 dB and an input-referred noise of 1.3 nV/$\sqrt{\text{Hz}}$ in the MICS and BCC bands while drawing 1.2 mA from the supply.

C. Current Recycling Concurrent Down-Conversion Mixer

The BCC and MICS signals amplified by the LNA need to be applied to separate down-conversion mixers driven by different LOs. Fig. 11 shows the circuit topology which makes the two mixers operate concurrently while consuming no extra current. The single-balanced active mixer shifts the frequency band of the MICS signal to 450 kHz with 10 dB gain. Abrupt switching of M_2 and M_3 is important for higher conversion gain and less noise injection to the output. Therefore, it is common to provide half of the bias current I_B of M_1 externally to reduce the current commutated by the switching transistors [15]. In this work, the extra current is recycled to activate a single-to-differential (STD) buffer driving the passive BCC mixer. The $R_C C_C$ low-pass filter decouples the two mixers by attenuating $>$ 200 mV signal fluctuation on M_1 drain to less than 0.1 mV at the output of the STD buffer. The resistance of R_C should be much higher than $1/g_m$ of M_2 or M_3 to minimize the amount of the signal current lost through R_C after amplification by the M_1 transconductor. However, the R_C cannot be arbitrarily large because the output swing level of the STD buffer is significantly limited owing to voltage drop of $R_C I_B/2$. Due to this tradeoff, the resistance of R_C is chosen as 2.5 kΩ which is 7 times as high as $1/g_m$ of M_2. The STD buffer with 15 dB gain compensates the loss incurred by passive mixing. In addition, the passive mixer is applicable to the direct-conversion RX for BCC since it introduces little flicker noise. According to simulations using two tones from the BCC and MICS bands, the concurrent operation has no effect on the input-referred noise of each mixer, and $<$ 2 dB degradation of the $P_{1\text{dB}}$ is observed.

D. Channel Selection Circuits

After the LNA/mixer cascade, the BCC and MICS baseband signals go through a fourth-order low-pass filter and a fifth-order complex band-pass filter, respectively for channel selection. The schematics of unit stages constituting the two baseband filters are shown in Fig. 12. For the simplicity, all circuits are represented in single-ended form although their actual implementations are fully differential. The complex integrator of Fig. 12(a) generates a complex pole at $-1/R_2C_2 + j/R_3C_2$. Because there is no conjugate pole in the third quadrant of the s-plane, the image signal which has negative frequency after down-conversion can be filtered out. The poles of the cascaded integrators are selected to get the Butterworth filter response. The filter gain of 9 dB is distributed to the first two stages for the smallest input-referred noise. The BCC signal down-converted to zero-IF does not suffer from the image issue, but the signal bandwidth changes from 14 MHz to 1.5 MHz for the variable AFH scheme. The biquad of Fig. 12(b) has resistor arrays programmable with 4 bits to move the conjugate poles and hence control the cut-off frequency of the filter. The unit gain frequency of the op-amp is set to 400 MHz to guarantee $>$ 70° phase margin with all configurations of the resistor arrays.

The image rejection of a complex filter is very sensitive to gain and phase errors of I/Q paths. The image rejection of 70 dB

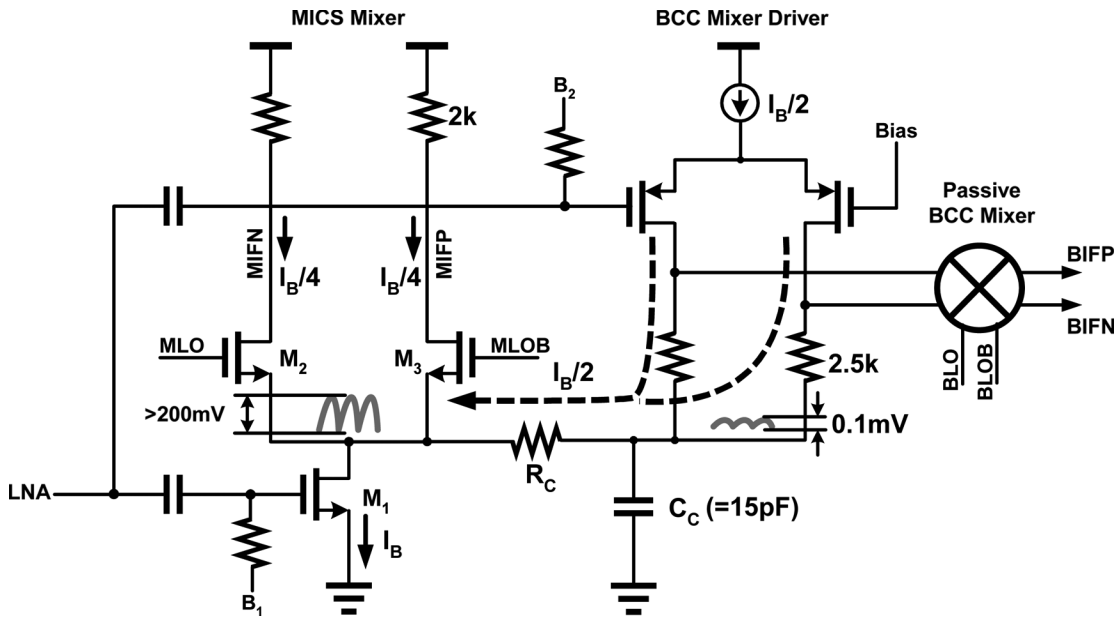

Fig. 11. Current-recycling dual-band mixer.

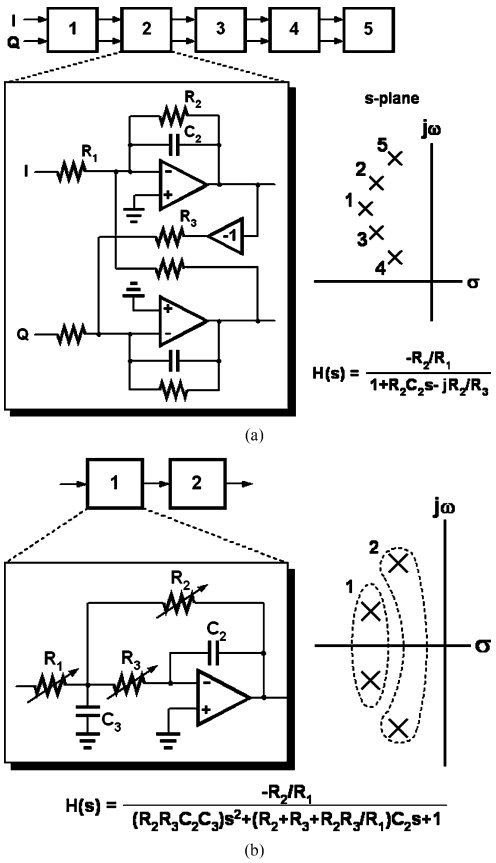

Fig. 12. Channel selection filters. (a) Unit stage of the fifth-order complex BPF. (b) Biquad of the fourth-order LPF.

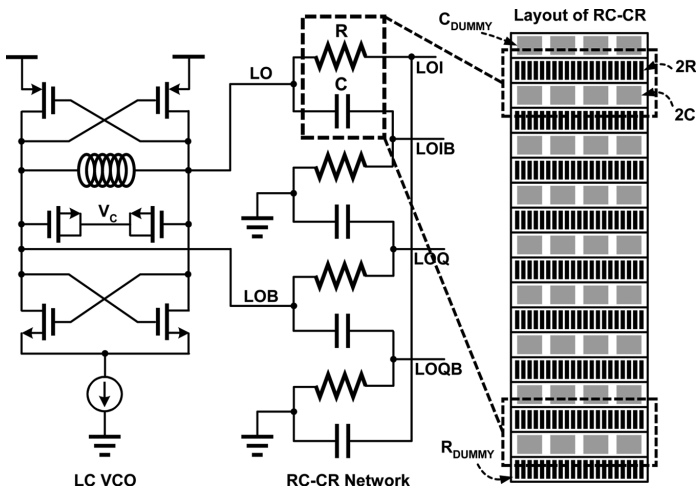

Fig. 13. I/Q LO generation circuit.

with perfect I/Q matching is reduced to 30 dB with just 3° phase or 1 dB gain imbalance. Fig. 13 shows the I/Q LO generation circuits utilized in this work. In contrast to using a divide-by-2 circuit or a quadrature VCO, adding an RC-CR network after the *LC* VCO requires much less operating power if Q factor of the *LC* tank is sufficiently high [16]. The I/Q accuracy of this circuit depends on harmonic components of the LO signal generated by the oscillator and matching among the resistors and capacitors employed. The off-chip inductor with high Q $(= 15)$ is driven by both of the nMOS and pMOS cross-coupled latches to generate the sinusoid with low distortion. As a result, the output of the *LC* VCO has the second and third harmonics below 33 and 35 dBc which contribute to 1° I/Q phase error. All resistors and capacitors constituting the RC-CR network are split and placed to compensate the linear gradient.

V. Implementation Results

The dual-band transceiver has been fabricated in 0.18 μm mixed-mode CMOS technology and the chip microphotograph is shown in Fig. 14. The total chip area including pads is 1.9×2.5 mm^2. The front-end circuits including LNA and mixer are common between BCC and MICS. The 5 inductors used in the

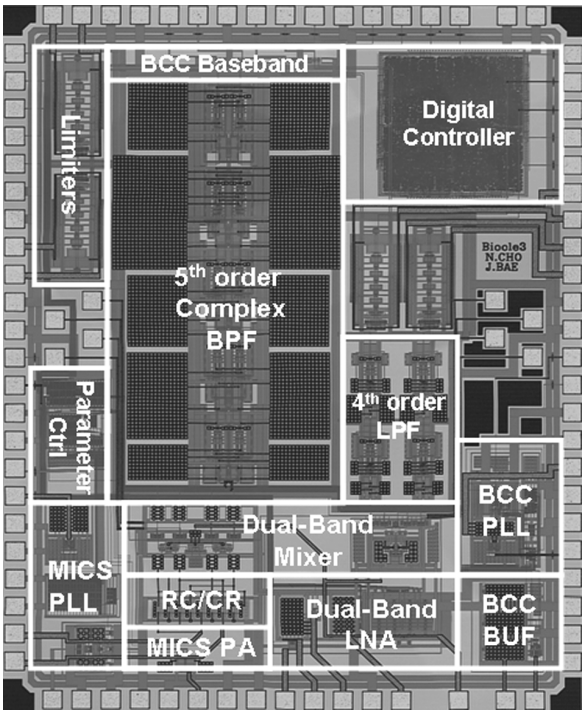

Fig. 14. Chip microphotograph (1.9×2.5 mm^2).

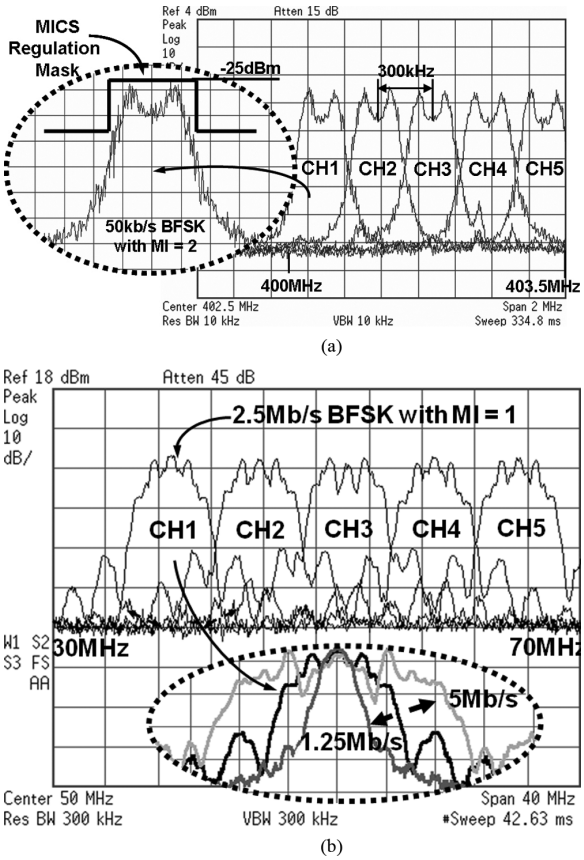

(a)

(b)

Fig. 15. TX output spectrums. (a) MICS TX spectrums. (b) BCC TX spectrums.

transceiver are off-chip devices whose Q factor is higher than that of an on-chip inductor. All circuit measurements are performed with a 1.8 V supply.

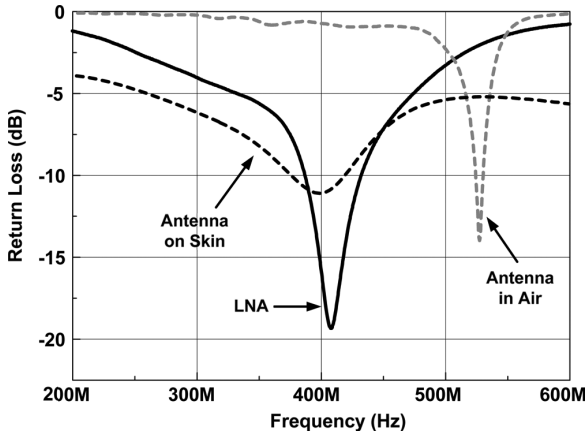

Fig. 16. Return losses of antenna and LNA.

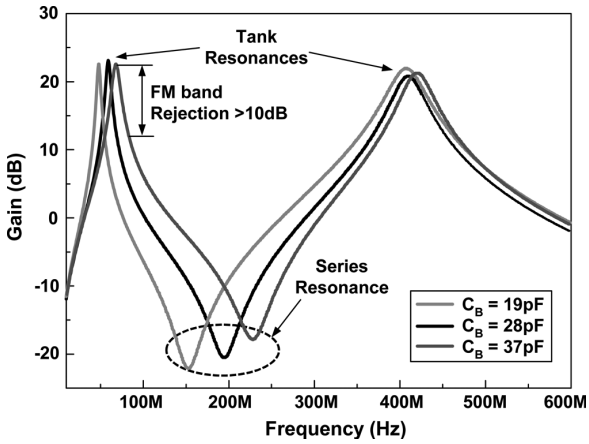

Fig. 17. LNA gain curve.

Fig. 15 shows the output TX spectrums. The 50 kb/s BFSK signals within the first five MICS channels are measured by a spectrum analyzer and superimposed as shown in Fig. 15(a). The frequency separation between the adjacent channels is 300 kHz and each spectrum satisfies the FCC regulation mask successfully [6]. The output power is currently set to -25 dBm, which is far less than the -16 dBm EIRP limit [6]. However, the power level can be raised up to 0 dBm to compensate the antenna loss. The power efficiency of the TX buffer is 33% at the operating point where the MICS TX outputs -5 dBm. Fig. 15(b) shows the BCC TX spectrums. For 2.5 Mb/s data rate, the 30–70 MHz band is divided into five channels and each channel is used for BFSK modulation with the MI of 1. As shown in the circle, the channel bandwidth can be varied from 3.5 to 14 MHz in proportion to TX data rate. This indicates that the variable AFH is possible by changing the number of hopping channels according to interference condition.

The return losses of the antenna and the dual-band LNA are shown in Fig. 16. Due to high electrical permittivity of the human tissue, the 530 MHz resonant frequency of the antenna in air is lowered to 400 MHz on the skin. The body conductivity of > 0.5 S/m contributes to dispersion of the return loss curve. The return loss of the inductively degenerated LNA is less than -15 dB over the 402–405 MHz MICS band. Therefore, the on-body antenna and LNA can be connected directly without any matching network. Fig. 17 is the measured LNA gain

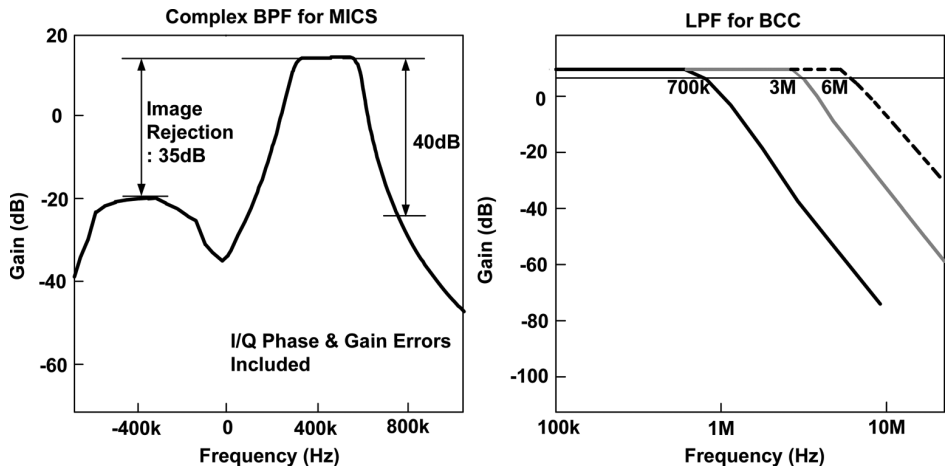

Fig. 18. Channel selectivity of the transceiver.

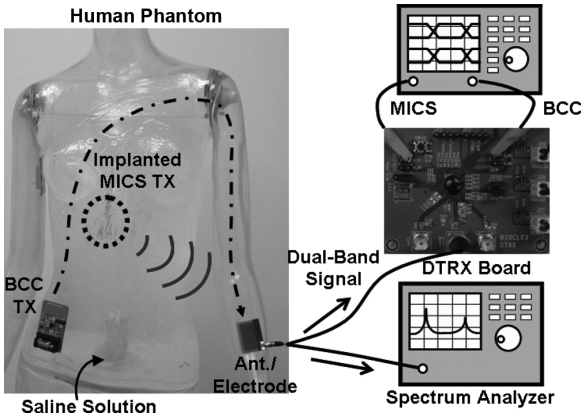

Fig. 19. Experimental setup for sensitivity measurement.

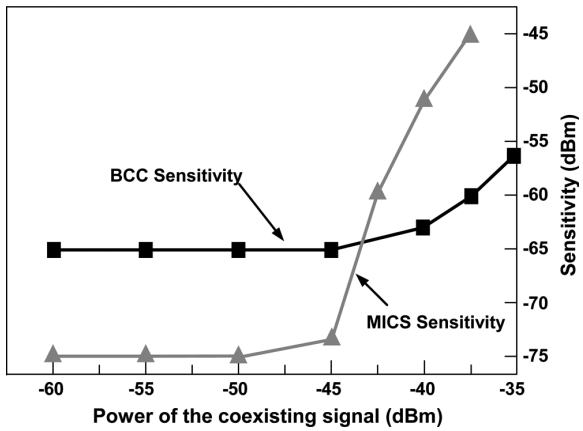

Fig. 20. Sensitivity under BCC and MICS signals coexistence.

as a function of frequency. The two tank resonances of the cascaded *LC* tanks provide $>$ 16 dB gains both in the BCC and MICS bands. The voltage gain at each BCC channel is kept above 16 dB thanks to the programmable capacitor and resistor arrays connected to the BCC inductor in parallel. The series resonance of the cascaded networks occurs around 200 MHz. This suppresses interferences such as FM radio signals coupled through the human body by more than 10 dB.

Fig. 18 shows the channel selectivity of the transceiver. In the MICS band, the adjacent channel rejection is 40 dB. The image signal is attenuated by 35 dB, which implies only 2° phase and 0.3 dB gain imbalances between I and Q signals. The cut-off frequency of the BCC low-pass filer is scalable to maintain its selectivity when the channel bandwidth changes for the variable AFH.

Fig. 19 shows the experimental setup to investigate how much the sensitivities of the BCC and MICS RXs are affected by coexistence of the dual-band signals during concurrent operation. The human phantom is prepared to make the communication channel. Its inner space is filled with saline solution which is often used to simulate the in-body environment, and its outer layer is processed to have the conductivity of the human tissue, which is around 0.6 S/m. The BCC TX on the phantom surface and the implanted MICS TX [5] are battery-powered and emit FSK signals. The BCC signal is electrically coupled to the dual-band transceiver through the conductive layer and the MICS signal in the form of electromagnetic wave propagates the saline solution and goes into the transceiver. The antenna combined with an electrode is an interfacing unit that receives the BCC and MICS signals concurrently and transfers them to the transceiver. The spectrum analyzer measures the power level of the received dual-band signal. The digital oscilloscope displays the BCC and MICS bit streams recovered concurrently. With this experimental setup, the sensitivity of the MICS RX is measured while moving the BCC TX toward the electrode to increase the strength of the BCC RX signal. The sensitivity of the BCC RX is also measured in the same way. As shown in Fig. 20, the BCC sensitivity is -65 dBm when the coexisting MICS signal is low enough. However, above -40 dBm of the MICS signal, the errors in the recovered BCC data start to appear due to the receiver saturation. For the MICS RX, the -75 dBm sensitivity is maintained up to -45 dBm BCC signal. In summary, the BCC and MICS RXs can withstand the 25 dB and 30 dB larger MICS and BCC signals without sensitivity degradation. Fig. 21 is the power breakdown of the RX. The BCC and MICS front-end circuits which consume the largest power are shared and hence 30% of the total operating power can be saved. The power consumption of the TX is 4.9 mW. Table I summarizes

TABLE I
PERFORMANCE SUMMARY.

Performance Parameters	[11]	This Work		[4]
		BCC	MICS	
Frequency Band	30 - 120MHz	30 - 70 MHz	402 - 405 MHz	402 - 405MHz
No. of Channels	4	3 - 20	10 (each 300kHz BW)	10
Interference Rejection Technique	AFH	Variable AFH	Listen-Before-Talk (LBT)	LBT
Interference Rejection	25dB	32dB	20dB	NA
Data Rate	60kb/s - 10Mb/s	500kb/s - 5Mb/s	50kb/s @ TX 200kb/s @ RX	200kb/s
Front - End Voltage Gain	36dB	34dB	36dB	NA
Sensitivity	-65 dBm	-65 dBm @ 2.5Mb/s	$35\mu V_{rms}$	$20\mu V_{rms}$
P_{1dB}	-40 dBm	-32 dBm	-25dBm	NA
TX Output Magnitude	1.5 V_{swing}	> 3V_{swing}	-20 - 0dBm	-17 - -4dBm
Power Consumption	BCC Only 3.7mW	BCC (2.3mW) + MICS (8.5mW) = 10.8mW		MICS Only 11.5mW

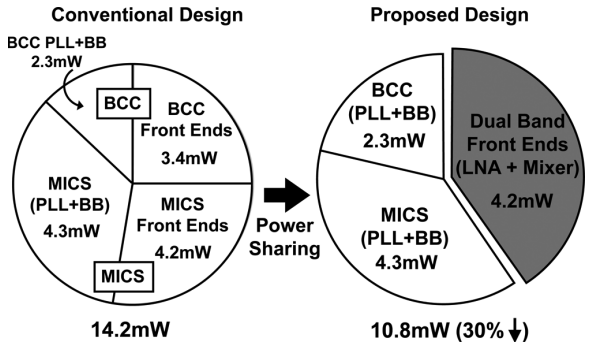

Fig. 21. RX power breakdown.

major performance parameters of the proposed transceiver and compares it with the conventional works. The dual-band transceiver satisfies all FCC regulations for MICS. Because coverage of the unified BSN is less than 1 m, the sensitivity of the dual-band transceiver is enough with 35 μV. Instead, the transceiver consumes less power than the commercial MICS radio even with the BCC function integrated. In the BCC mode, this work outperforms the previous BCC transceiver in most parameters.

VI. CONCLUSION

This work presents a dual-band transceiver that can communicate with various wireless sensors on and inside human body for the unified BSN. The transceiver operates in 30–70 MHz band for BCC and 402–405 MHz band for MICS. For low energy consumption of the transceiver, the front-end circuits shared between BCC and MICS receives dual-band signals concurrently without spending additional current. Hence, up to 30% of the total energy is reduced. To support the concurrent operation, the dual-band LNA incorporates cascaded *LC* tanks which provide $>$ 16 dB gains both in the BCC and MICS bands. The current-recycling mixer down-converts the BCC signal to zero-IF and the MICS signal to 450 kHz-IF concurrently. The cut-off frequency of the low-pass filter for BCC is programmable to maintain its adjacent channel rejection as $>$ 30 dB with the variable signal bandwidth. The complex filter for MICS provides 38 dB and 40 dB image and adjacent channel rejections, respectively. The transceiver implemented with 0.18 μm CMOS satisfies all FCC regulations for MICS and consumes 10.8 mW during the concurrent operation.

REFERENCES

[1] Body Area Networks (BAN), IEEE 802.15 WPAN™ Task Group 6, Nov. 2007 [Online]. Available: http://www.ieee802.org/15/pub/TG6.html

[2] N. Cho, J. Bae, S. Kim, and H. J. Yoo, "A 10.8 mW body-channel-communication/MICS dual-band transceiver for a unified body-sensor-network controller," in *IEEE Int. Solid-State Circuits Conf. Dig. Tech. Papers*, 2009, pp. 424–425.

[3] D. M. Pozar, *Microwave Engineering*, 3rd ed. Hoboken, NJ: Wiley, 2005.

[4] P. D. Bradley, "An ultra-low-power high-performance medical-implant-communication-system transceiver for implantable devices," in *Proc. IEEE Biomedical Circuits and Systems Conf.*, 2006, pp. 158–162.

[5] J. Bae, N. Cho, and H. J. Yoo, "A 490 μW fully MICS compatible FSK transceiver for implantable devices," in *Symp. VLSI Circuits Dig. Tech. Papers*, 2009, pp. 36–37.

[6] FCC Rules and Regulations, MICS Band Plan, Part 95, 2003.

[7] A. C. W. Wong *et al.*, "A 1 V, micropower system-on-chip for vital-sign monitoring in wireless body sensor networks," in *IEEE Int. Solid-State Circuits Conf. Dig. Tech. Papers*, 2008, pp. 138–139.

[8] B. Gosselin, L. Faniel, and M. Sawan, "A high data rate telemetry system for multi-channel biosignal recording," in *Proc. IEEE Biomedical Circuits and Systems Conf.*, 2006, pp. 170–173.

[9] A. Fort *et al.*, "Ultra-wideband channel model for communication around the human body," *IEEE J. Sel. Areas Commun.*, vol. 24, no. 4, pp. 927–933, Apr. 2006.

[10] S. J. Song *et al.*, "A 0.9 V 2.6 mW body-coupled scalable PHY transceiver for body sensor applications," in *IEEE Int. Solid-State Circuits Conf. Dig. Tech. Papers*, 2007, pp. 366–367.

[11] N. Cho, L. Yan, J. Bae, and H. J. Yoo, "A 60 kb/s-10 Mb/s adaptive frequency hopping transceiver for interference-resilient body channel communication," *IEEE J. Solid-State Circuits*, vol. 44, no. 3, pp. 708–717, Mar. 2009.

[12] N. Cho *et al.*, "Human body characteristics as a signal transmission medium for intrabody communication," *IEEE Trans. Microw. Theory Tech.*, vol. 55, no. 5, pp. 1080–1086, May 2007.
[13] RSS-243 Active Medical Implants Operating in the 402-to-405 MHz Band, 2005 [Online]. Available: http://www.ic.gc.ca/epic/site/smt-gst.nsf/vwapj/rss243e.pdf/$FILE/rss243e.pdf
[14] P. Soontornpipit, C. M. Furse, and Y. C. Chung, "Design of implantable microstrip antenna for communication with medical implants," *IEEE Trans. Microw. Theory. Tech.*, vol. 52, no. 8, pp. 1944–1951, Aug. 2004.
[15] B. Razavi *et al.*, "A UWB CMOS transceiver," *IEEE J. Solid-State Circuits*, vol. 40, no. 12, pp. 2555–2562, Dec. 2005.
[16] A. Tekin, M. R. Yuce, and W. Liu, "Integrated VCO design for MICS transceiver," in *Proc. IEEE Custom Integrated Circuits Conf.*, 2006, pp. 765–768.

Namjun Cho (S'04) received the B.S. (*summa cum laude*) and M.S. degrees from KAIST, Korea, in 2004 and 2006, respectively. He is currently working toward the Ph.D. degree at KAIST.

He has worked on developing UHF RFID tag chip integrated with environmental monitoring sensors and the low-power digital-to-analog converter for hearing aid systems. His current research interests include low-power biomedical microsystems and the wireless transceivers for communication among wearable and implantable health care devices.

Joonsung Bae (S'07) received the B.S. degree in electrical engineering and computer science from KAIST, Korea, in 2007. He is currently working toward the M.S. degree in electrical engineering and computer science at KAIST.

His current research interests include high-speed and low-energy on-chip global interconnects and low-power CMOS transceiver design for Body Area Networks.

Hoi-Jun Yoo (M'95–SM'04–F'08) graduated from the Electronic Department of Seoul National University, Seoul, Korea, in 1983 and received the M.S. and Ph.D. degrees in electrical engineering from the Korea Advanced Institute of Science and Technology (KAIST), Daejeon, in 1985 and 1988, respectively. His Ph.D. work concerned the fabrication process for GaAs vertical optoelectronic integrated circuits.

From 1988 to 1990, he was with Bell Communications Research, Red Bank, NJ, where he invented the two-dimensional phase-locked VCSEL array, the front-surface-emitting laser, and the high-speed lateral HBT. In 1991, he became a manager of the DRAM design group at Hyundai Electronics and designed a family of fast-1M DRAMs to 256M synchronous DRAMs. In 1998, he joined the faculty of the Department of Electrical Engineering at KAIST and now is a full Professor. From 2001 to 2005, he was the Director of System Integration and IP Authoring Research Center (SIPAC), funded by Korean Government to promote worldwide IP authoring and its SOC application. From 2003 to 2005, he was the full-time Advisor to Minister of Korea Ministry of Information and Communication and National Project Manager for SoC and Computer. In 2007, he founded System Design Innovation and Application Research Center (SDIA) at KAIST to research and to develop SoCs for intelligent robots, wearable computers and bio systems. His current interests are high-speed and low-power Network on Chips, 3-D graphics, Body Area Networks, biomedical devices and circuits, and memory circuits and systems. He is the author of the books *DRAM Design* (Hongleung, 1996; in Korean), *High Performance DRAM* (Sigma, 1999; in Korean), *Low-Power NoC for High-Performance SoC Design* (CRC Press, 2008), and chapters of *Networks on Chips* (Morgan Kaufmann, 2006).

Dr. Yoo received the Electronic Industrial Association of Korea Award for his contribution to DRAM technology in 1994, the Hynix Development Award in 1995, the Design Award of ASP-DAC in 2001, the Korea Semiconductor Industry Association Award in 2002, the KAIST Best Research Award in 2007, and the Asian Solid-State Circuits Conference (A-SSCC) Outstanding Design Awards in 2005, 2006 and 2007. He is an IEEE Fellow and serving as an Executive Committee Member and the Far East Secretary for IEEE ISSCC, and a Steering Committee Member of IEEE A-SSCC. He was the Technical Program Committee Chair of A-SSCC 2008.